



Article

Selective Fabrication of Barium Carbonate Nanoparticles in the Lumen of Halloysite Nanotubes

Jing Ouyang ^{1,2,3,*} , Dawei Mu ^{1,2}, Yi Zhang ^{1,2}, Huaming Yang ^{1,2}  and Steven L. Suib ³

¹ Key Laboratory for Mineral Materials and Application of Hunan Province, Central South University, Changsha 410083, China; mudawei@csu.edu.cn (D.M.); yee_z10@csu.edu.cn (Y.Z.); hmyang@csu.edu.cn (H.Y.)

² Centre for Mineral Materials, Department of Inorganic Materials, School of Minerals Processing and Bioengineering, Central South University, Changsha 410083, China

³ Department of Chemistry, Unit 3060, University of Connecticut, Storrs, CT 06269-3060, USA; steven.suib@uconn.edu

* Correspondence: jingouyang@csu.edu.cn; Tel.: +86-731-8883-0549; Fax: +86-731-8871-0804

Received: 21 May 2018; Accepted: 4 July 2018; Published: 11 July 2018



Abstract: Barium carbonate (BaCO_3) materials with the controllable morphology of nanoparticles were selectively loaded into the lumen halloysite nanotubes (abbreviated as Hal) by a urease assisted catalytic implementation strategy. The Hal mineral was pre-treated through leaching by hydrochloric acid (abbreviated as A-Hal), resulting in increased defect sites and zeta potential. The negatively charged urease was loaded inside the positively charged A-Hal lumen, and then through the decomposition of urea catalyzed by urease to produce carbonate ions and ammonia. When Ba^{2+} diffused in, BaCO_3 particles were selectively synthesized in the lumen of A-Hal, the pore channels of A-Hal effectively controlled the growth and aggregation of BaCO_3 nanocrystals and their geometrical morphology. The obtained BaCO_3 /A-Hal-T was characterized by transmission electron microscopy, Fourier transformation infrared spectroscopy and X-ray diffraction, differential scanning calorimetry-thermogravimetry (DSC-TG). The BaCO_3 /A-Hal-T may provide a candidate for potential applications.

Keywords: halloysite; urease; barium carbonate; selective decoration; nanoreactors

1. Introduction

Halloysite (abbreviated as Hal) ($\text{Al}_2\text{Si}_2\text{O}_5(\text{OH})_4 \cdot 2\text{H}_2\text{O}$) is a kind of clay mineral in the category of the kaolin group. These two have similar chemical compositions and analogous crystallographic structures. While unlike the kaolinite crystals, the layers in Hal are naturally curved to form a tubular structure due to the size mismatch of the two kinds of polyhedra [1,2], yielding the naturally occurred nano-tubular morphology in the Hal minerals. The outer silicon (hydr)-oxide tetrahedral [SiO_4] surface and the interior aluminum (hydr)-oxide octahedral [AlO_6] surface are arranged in a layer-by-layer 1:1 manner [3]. The chemical difference between the inner and outer surface of Hal result in a negative charged external surface and a positive charged interior surface in a wide pH range of 3.0~9.0 [3]. So, Hal has a negative overall zeta potential from $-50 \sim -30$ mV in this pH range, which makes the very good dispersion and colloidal stability of Hal in mild acidic circumstances [4]. The length of Hal varies between 100~1000 nm, the interior and external diameter are about 15~20 nm and 50~80 nm, respectively [5,6]. Hal has many unique properties such as high surface area, high aspect ratio, high porosity, large surface chemical properties, non-toxic biocompatibility and good thermal stability [7], etc., making Hal widely used as a hydrogen storage matrix [8–10], catalysis supports [11–19], nanoreactors [20–22], medicine carrier, biological antibacterial [4,23–26]

and other functional materials [27–32]. Some excellent reviews have summarized the physical and chemical properties of Hal with structural modification methods and have included the applications of the Hal-based materials [33–36].

BaCO₃ is a thermodynamically stable crystal among the carbonates existing in nature. BaCO₃ has recently attracted a lot of research [37] due to its close relationship with many important applications in the ceramic and glass industries, as well as a precursor for magnetic ferrites and/or ferroelectric materials [38]. Recently, the application of BaCO₃ nanoparticles as catalysts for high-temperature oxygen reduction reactions (ORR) in solid oxide fuel cells (SOFCs) was reported [39,40]. Then, Cao et al. showed that the barium ions on the surface of catalyst played a key role in the adsorption of oxygen molecules and the formation/decomposition of intermediates for ORR [41]. Cai et al. found that the BaCO₃/CaO composite after additive roasting and acid leaching was proved to be feasible for vanadium recovery from refractory stone coal [42]. The influence of BaCO₃ on chlorine fixation and combustion characteristics was investigated by Wang et al. and showed that the chlorine fixation of cotton stalk was improved 5.35 times by adding a reasonable ratio of BaCO₃. The reasonable additive ratio between biomass, NH₄H₂PO₄ and BaCO₃ could be K:P:Ba = 1:1.5:1 [43]. Zhang et al. chose BaCO₃ as the support of Ag-CuCl₂ catalyst for gas-phase epoxidation of propylene by oxygen; the composite catalyst showed fairly good propylene oxidation (PO) selectivity and propylene conversion efficiency [44]. Whittaker et al. studied the multi-step crystallization, rapid interconversion of amorphous and crystalline precursors of barium carbonate [45]. Massoni et al. studied the effect of BaCO₃ on the synthesis of barytocalcite, which showed that barium carbonate has positively affected the sintering processes through decreasing the sintering activation energy and increasing the shrinkage rate to obtain higher densities [46]. Zhang et al. found that barium carbonate can be used in solar power plants for high-temperature thermal energy capture, transportation and storage materials [47]. The above literature clearly shows the high importance of barium carbonate in the fields of both mineralogical and materials science. In addition, BaCO₃ is a widely available and very cheap material that has attracted much attention in applications as catalysts for high-temperature oxygen reduction in solid oxide fuel cells (SOFC). The BaCO₃ nanoparticles can obviously decrease the interfacial polarization resistances of cathodes for medium-temperature SOFCs. About one order of magnitude resistance reduction is originated from the low-frequency response [39]. Barium ions on the surface of catalyst play a key role in the adsorption of oxygen molecules and the formation/decomposition of intermediates [41]. Therefore, infiltrating the electrocatalyst (BaCO₃) within a porous structure (such as the Hal minerals with naturally occurred nanotubes) may increase the catalytic activity through elevating the surface area as well as reducing the aggregation of the catalyst [40]. However, there are few reports on synthesizing BaCO₃ in mineral based matrices, especially in the lumen of tubular Hal to the best of our knowledge.

Here, the BaCO₃ nanoparticles with controlled morphology are prepared in tubular channels of halloysite through a urease assisted catalytic assembly strategy. Hydrochloric acid treatment to halloysite is conducted in order to expand the diameter of the nanotubes, and so as to facilitate the anchoring of biological active catalyst (urease) in the lumen of A-Hal. The urease is introduced as the key component to accelerate the decomposition of urea to carbonate ions and facilitate barium carbonate precipitation in the tubes. The inner lumen of halloysite plays the role of nano-confinement for BaCO₃ nanoparticles (2~8 nm). The synthesis of BaCO₃/A-Hal-T in this work is of value in the field of controllable assembly of functional materials in a tubular template for many potential applications.

2. Experimental

2.1. Materials

Hal was obtained from Linfen, Shanxi province in China. Visible impurities attached on the raw mineral (such as the brown parts containing too much ferrites and soil) were removed by manual selection, white or blue bulks were ground and passed a 200 Mesh sieve. In the pretreatment process,

10 g Hal raw mineral was dissolved in 500 mL deionized water and magnetically stirred at 600 rpm for 6 hours. Finally, after standing for 10 hours, the supernatant was centrifuged and washed by ethanol, followed by drying at 60 °C. Urease (MW 480,000, diameter 5 nm [48]) from Jack Bean was purchased from Aladdin Reagent Co., Ltd. (Shanghai, China). BaCl₂ and urea were purchased from Sinopharm Chemical Reagent Co., Ltd. (Shanghai, China). All other reagents in this study were analytically pure and were used as received without further purification.

2.2. Acid Treating

The pretreated Hal (1 g) was added into 50 mL 2 M hydrochloric acid solution (HCl), and subsequently magnetically stirred in a conical flask at 60 °C for 5 h. The aim of acid leaching was to partially dissolve the aluminum in the tube and expand diameter of the lumen to facilitate the assembly of urease molecular and metal resources. The suspension was then filtered and washed with distilled water for several times to remove all of the leached Al³⁺ and residual Cl[−] ions until no acid could be detected by AgNO₃ solvent. The treated mineral was dried at 60 °C to obtain the acid-treated Hal sample (denoted as A-Hal). Then A-Hal were ground and passed through a 200 Mesh sieve before being used.

2.3. Experimental Procedure

The acid-treated Hal was mixed with urease solvent (12.5 mg/mL), the solution was magnetically stirred for 30 min and then the suspension was transferred into a vacuum jar, a pump was used to vacuum the chamber. Slight fizzing of the suspension suggested the air interior of the halloysite lumen was removed. After the fizzing stopped, the vial was sealed for 30 min to reach an equilibrium enzyme distribution [20]. The process was repeated twice. The modified halloysite underwent extensive washing/centrifugation with distilled water to remove excessive urease solvent from the outer surfaces of the nanotubes. After that, the Hal with urease molecules was dispersed ultrasonically in a mixture of urea (0.0025 M) and BaCl₂ (0.005 M) for 30 min and transferred to a vacuum jar to repeat the pump steps. After the reaction, the halloysite suspension was centrifuged to remove excess of the Ba-salt and the process was repeated two times to ensure that the halloysite was filled with the maximum amount of barium carbonate. The product was dried at 60 °C, BaCO₃/A-Hal was calcined at 500 °C to remove residual organics (denoted as BaCO₃/A-Hal-T).

2.4. Characterizations

The phase of the samples was confirmed with a powder X-ray diffractometer (DX-2700, Dandong Hao Yuan Apparatus Co., Ltd., Dandong, China) with Cu K α -radiation ($\lambda = 1.541806 \text{ \AA}$). Sample was scanned from 5° to 80° of 2θ with a step width of 0.02°. The zeta potential was measured on a Zeta potential and Size Distribution Analyzer Zeta plus (Malvern Zetasizer NANO ZS90, Malvern, Malvern, UK). The clay was dispersed in distilled water at a concentration of 5 mg/mL, prior to the tests, the Hal and A-Hal samples were stirred and soaked in the testing solution for a minimum of 30 min to guarantee the sufficient infiltration by the solvent. HCl (0.5% wt %) and NaOH (1% wt %) were used to adjust the pH to the range 2.0–12.0. Fourier transform infrared spectroscopy (FTIR) analysis was performed at room temperature using a Bruker TENSOR27 spectrometer from 4000 cm^{−1} to 400 cm^{−1} with pressed disks of the sample and KBr mixture (the mass ratio is 1:100). A TESCAN MIRA3 LMU scanning electron microscope was used to observe the surface morphologies. The resolution of the secondary electron image was 1.0 nm, the acceleration voltage was adjustable in the range of 0.2–30 kV, the magnification was 3.5–1,000,000 times. Transmission electron microscopy (TEM) images were characterized with a TEM system (Titan G2 60-300, FEI, Hillsboro, OR, USA) operated at 200 kV, which was equipped with an energy-dispersive X-ray spectrometer (Oxford EDX, Oxford, UK). The contents of Ba in the sample were measured with an inductively coupled plasma emission spectrometer (ICP-AES) on a Thermo Scientific-ICAP 7400 spectrometer (Thermo Scientific, Waltham, MA, USA). TG/DSC (Mettler Toledo, Zurich, Switzerland) curves of the samples were measured by a Mettler Toledo TGA/DSC3+ /1600 LF in Nitrogen atmosphere, the heating rate was set at 10 °C/min.

3. Results and Discussion

Surface charge characters of the raw mineral and acid-treated Hal should have great influence on the successful assembly of urease and barium sources. Therefore, the Zeta potential test is used before the synthesis process to determine the surface double-layer electronic potential of the pristine and acid-treated Hal minerals (Figure 1). In a wide range of pH values, the surface potential of the Hal exhibits a large net negative charge, the potential decreases when pH is adjusted to 2.0. After acid treatment, the zeta potential of the A-Hal relatively increases, but still remains negatively charged [49]. The over-all negative charge of halloysite should be reasoned as follows: During the acid leaching process, the aluminol Al–OH species on the surface of the Hal is protonated by the H^+ ions in the acid solution, forming a positive Al(OH₂) species. These positive species will weaken the bonding between Al and O atoms, resulting in the partial leaching of Al from Hal. The Al content in each aluminosilicate layer will decrease from the inner shell to the outer shell, and thus would expand the multilayer structure within the tube lumen [50]. After acid activation, Hal shows a disaggregated tube morphology and the nanotubes are broken into smaller tubes. Hydroxyl groups located at edges, steps, and related defects of clay mineral particles are different and called terminal OH groups. These OH groups are under-coordinated and carry either a positive or negative charge depending on the type of metal ion and the pH of the ambient aqueous solution [51]. Homogeneous substitution in halloysite is weakened during the acid leaching process, resulting in the rise of the overall zeta potential for A-Hal.

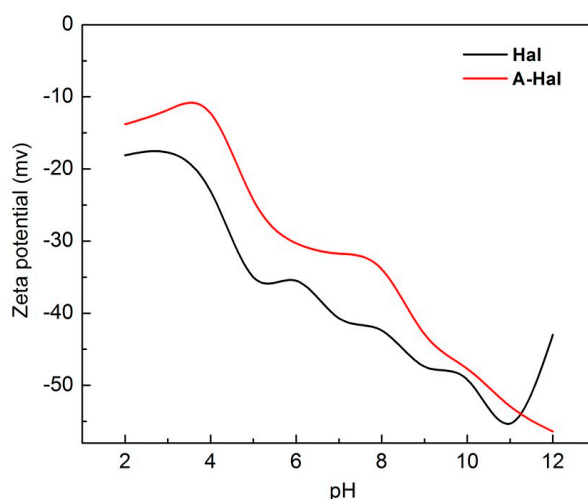


Figure 1. Zate potential plot of the Hal and A-Hal samples.

The X-ray diffraction pattern for pristine Hal in Figure 2 shows a number of peaks that can be well indexed to a typical 7 Å-halloysite (JCPDS PDF No. 29-1487, Hexagonal, space group *Primitive*), the diffraction peaks of A-Hal coincide well with the raw Hal. But after the acid treatment, the diffraction peaks of the halloysite are broadened, indicating the decreased crystallinity of the lattice. The lattice etching takes place at the interior layer during acid leaching, where aluminum ions are leached out, resulting in the mismatches and defects in the lattice of the A-Hal compared with the Hal. The XRD pattern of BaCO₃/A-Hal-T sample shows broad peaks at 23.89°, 24.30°, 27.71°, 34.07°, 41.98°, and 44.88°, relatively, which are characteristic peaks of BaCO₃ (JCPDS PDF No. 45-1471, orthorhombic, space group *Pnma*). No peak belongs to any impurities, confirming the relative high purity of the products.

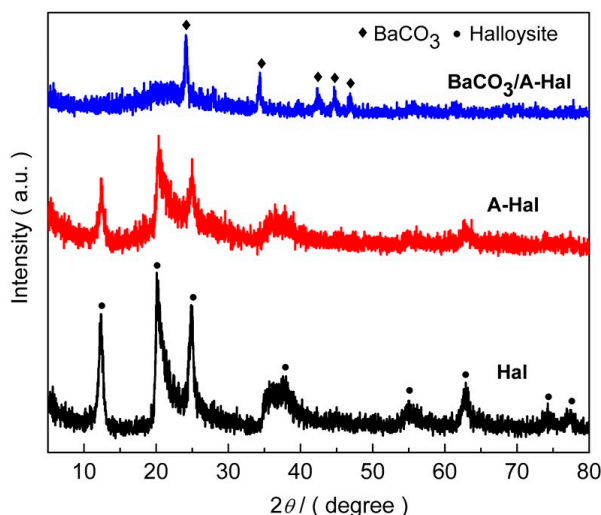


Figure 2. XRD patterns of the raw and acid-treated Hal mineral, and BaCO₃/A-Hal-T.

FTIR analysis in Figure 3 is further carried out to verify the formation of barium carbonate during the reaction process. Positions and assignments of the FTIR vibration bands of different samples are presented in Table 1. Both of the double peaks at 3697 and 3623 cm^{−1} are ascribed to the stretching vibrations of the adsorbed water in Hal, but the peak at 3697 cm^{−1} is the stretching vibrational mode of perpendicular surface −OH groups, and 3623 cm^{−1} is the stretching vibrational mode of inner hydroxyl groups, respectively [52]. The sharp peak at 1642 cm^{−1} corresponds to the H–O–H deformation band in the adsorbed water. Peak at 1032 cm^{−1} could be ascribed to the asymmetric in-plane Si–O–Si stretching. The adsorption peak at 910 cm^{−1} results from the −OH deformation of inner hydroxyls [53]. The sharp peak at 794 cm^{−1} corresponds to the symmetric stretching of Si–O. The spectral band at 691 cm^{−1} originates from the perpendicular stretching of Si–O bonds probably coordinated to surface hydroxyls. The double adsorption peaks at 534 cm^{−1} and 468 cm^{−1} are ascribed to the bending vibrations of the Si–O groups [54]. The former should result from the deformation of Al–O–Si frames, and the latter should have originated from the deformation of Si–O–Si bonds. According to the FTIR spectra of the Hal and A-Hal, the amount of Al–OH species decrease with a longer leaching time, as indicated by the weakness of the peaks at 3697, 3623 (Al–OH stretching vibrations), and 910 cm^{−1} (Al–OH deformation vibration). The peak at 1657 cm^{−1} could be attributed to C=O stretching mode of urease (amide I) [21]. The band observed at 1545 cm^{−1} corresponds to the stretching and deformation mode of N–H (amide II). The band at 1400 cm^{−1} is due to C–H vibrations of the CH₂ groups [55]. This red shift (urease) indicates that urease could form the interaction with aluminol (Al–OH) groups in the lumen of A-Hal. The IR spectra of BaCO₃/A-Hal-T exhibit adsorption peaks at around 1450, 856 and 694 cm^{−1}, which represent a characteristic absorbance of BaCO₃ with high purity. A wide and smooth absorption band at 3450 cm^{−1} is due to intermolecular hydrogen bonds or the stretching vibration peaks of O–H in water molecules. The peak at 694 cm^{−1} should result from in-plane bending vibrations of CO₃^{2−}; the peak at 856 cm^{−1} is ascribed to out-of-plane bending vibrations of CO₃^{2−}. The peak at 1450 cm^{−1} corresponds to the non-stretching vibrations of CO₃^{2−} [44]. These results are consistent with the XRD results of Hal and BaCO₃/A-Hal-T.

The thermal properties of the A-Hal, (b) U/A-Hal, (c) BaCO₃/A-Hal-T are recorded by TG and DSC from room temperature to 1100 °C at a heating rate of 10 °C/min (Figure 4). The TG curves of the A-Hal show two-stepped curves, the first step with about 2.98% weight loss before 150 °C is ascribed mainly to dehydration, including removal of the physically adsorbed water and the interlayer water during the transformation from Halloysite-10 Å to Halloysite-7 Å [54]. The second step about 13.47% and 14.83% weight loss in the range of 400–550 °C corresponds to the endothermic peak centered at 525 °C and 523 °C, respectively, and can be attributed to dehydroxylation in A-Hal and U/A-Hal [56].

The narrow exothermic peak at 997 °C is attributed to the phase segregation of SiO₂ and γ-Al₂O₃ from the halloysite lattice in the mineral [7]. The thermal decomposition of urease is considered to occur at 180 °C attributable to the fragments CONH and CHO, respectively, from the urease skeleton (Figure 4b). This temperature is higher than that observed for free urease, which suggests that the urease loaded in A-Hal is thermally stabilized. The decomposition products with higher molecular weight losses of about 7.22% are observed at 330 °C, which result from the thermal decomposition of residual amino acids of urease [57]. Figure 4c shows the TG-DSC curves of BaCO₃/A-Hal-T, which have a continuous weight loss of 6.01% from 25 to 800 °C, which may have originate from the desorption of water molecular before 200 °C, de-hydroxylation and decomposition of residual urea and urease, as well as possible carbonates before 800 °C.

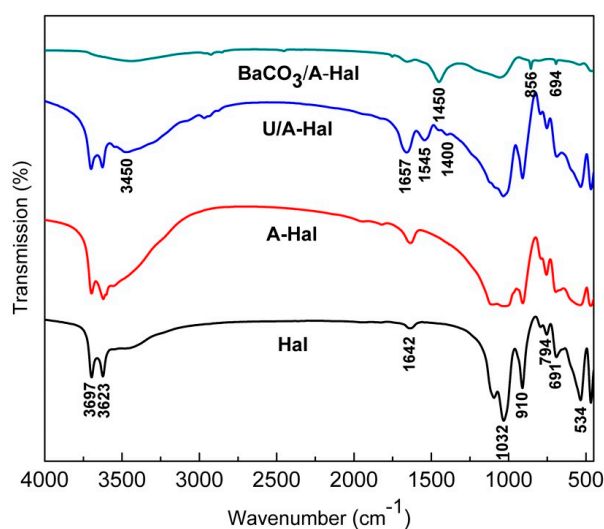


Figure 3. FTIR spectra of the raw Hal, A-Hal, U/A-Hal and BaCO₃/A-Hal-T samples.

Table 1. Positions and assignments of the FTIR vibration bands of different samples.

Position/cm ^{−1}	Assignments
3739	−O−H stretching of adsorbed water
3695	stretching of perpendicular surface −O−H
3624	−O−H stretching of inner hydroxyls
3450	stretching vibration peaks of O−H in water molecules
1642	bending of −OH in adsorbed water
1040	(Broad band) Si−O stretching
911	−O−H deformation of inner hydroxyls
691	perpendicular Si−O stretching
535	bending deformation of Al−O−Si
1657	stretching and deformation mode of C=O (amide I)
1545	stretching and deformation mode of N−H (amide II)
1400	C−H vibrations of the CH ₂ group
1450	non-stretching vibration of CO ₃ ^{2−}
856	out-of-plane bending vibration of CO ₃ ^{2−}
794	symmetric stretching of Si−O
694	in-plane plane bending vibration of CO ₃ ^{2−}

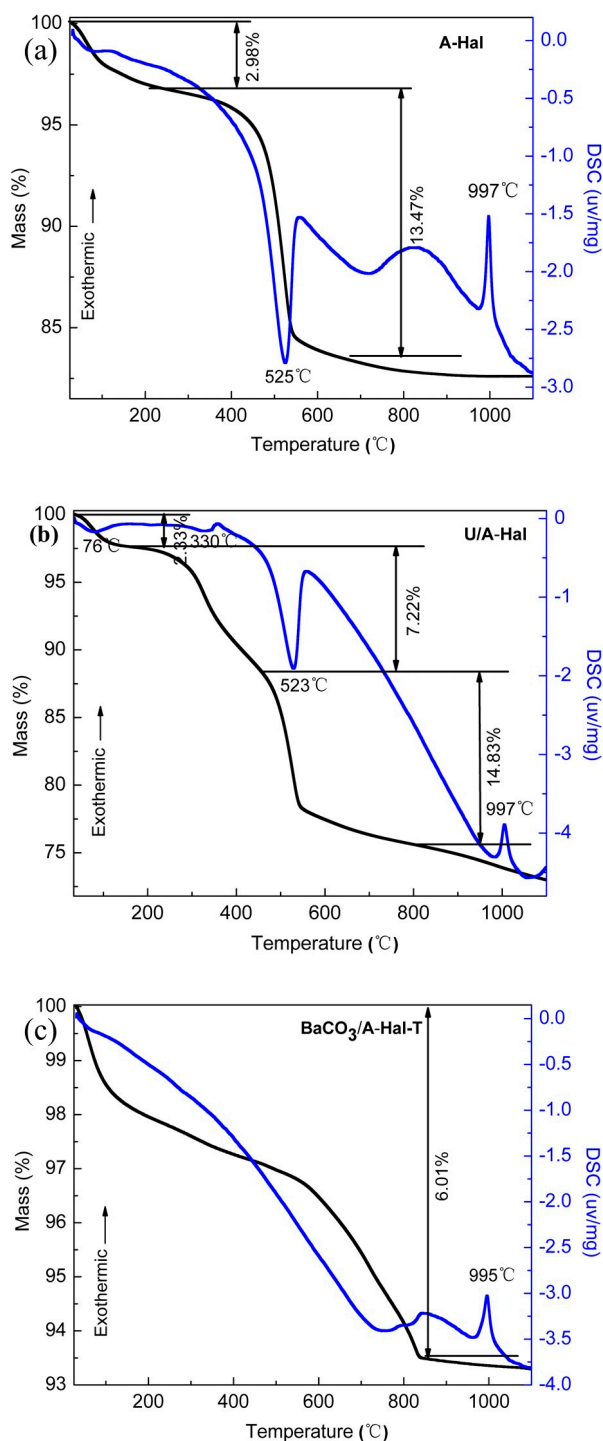


Figure 4. TG-DSC curves of (a) A-Hal, (b) U/A-Hal and (c) BaCO₃/A-Hal-T samples.

The scanning electron microscopy (SEM) micrographs verify that Hal has a rod like morphology (Figure 5a) with diameters of 30~50 nm and lengths of about 1000 nm. After acid leaching (Figure 5b), A-Hal shows a disaggregated tube morphology, the nanotubes are broken into smaller tubes, and the dispersibility of the Hal in the experiments is increased, which may result in a substantially short diffusion path. Hal contains the following major elements: O, Al, and Si. In addition, A-Hal mainly contains Si and O, while part of the Al content is retained (see the inset of Figure 5d). The external diameters of the tubes remain unchanged, indicating that etching takes place solely

in the inner lumen. The $\text{BaCO}_3/\text{A-Hal-T}$ in Figure 5c shows the nanotubes with similar character with that of the acid-treated Hal sample; few particles can be found on the outer surface of the nanotubes. Energy-dispersive X-ray analysis shows a small amount of Ba species in the products, confirming Ba-containing compound formation (Figure 5d). The total amount of released Ba ions from $\text{BaCO}_3/\text{A-Hal-T}$ is about 11.3% according to the ICP-AES analysis, which agrees well with the corresponding results of the SEM.

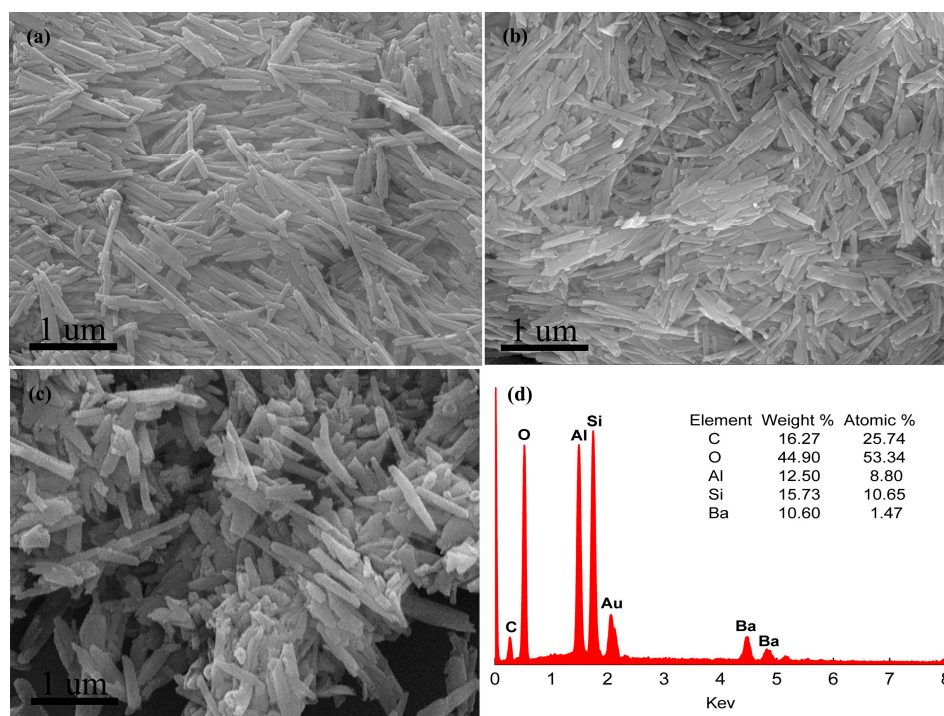


Figure 5. (a) SEM image of Hal, (b) A-Hal, (c) $\text{BaCO}_3/\text{A-Hal-T}$ and (d) EDX spectrum of $\text{BaCO}_3/\text{A-Hal-T}$.

The TEM images are acquired to further verify that barium carbonate particles are synthesized in the lumen of nanotubes from natural halloysite (Figure 6). A typical TEM image of Hal in Figure 6a shows that the pristine mineral possesses a hollow tubular structure with a smooth surface, open ends and continual hollow lumen with a diameter of about 15–30 nm and length of about 1000 nm. The acid-treated Hal (Figure 6b) is well dispersed in the copper mesh, and the sizes of A-Hal are a bit smaller than pristine Hal. Characteristics of tubular morphology are retained even after acid leaching, with diameters of the inside channel increasing about 10%, while the outer diameter of the tube remains unchanged, indicating that etching only occurs in the interior lumen. The observations of the crystal growth of the BaCO_3 nanoparticles (Figure 6c) suggest that the nanoparticles could be formed in A-Hal lumens, rather than attaching onto the external surface of A-Hal. The large amount of production of 2–8 nm sized BaCO_3 nanoparticles is observed in the lumen. The EDX spectrum in Figure 6d confirms that the sample contains Ba, Si and Al elements. All of these agree well with the corresponding FTIR and XRD results.

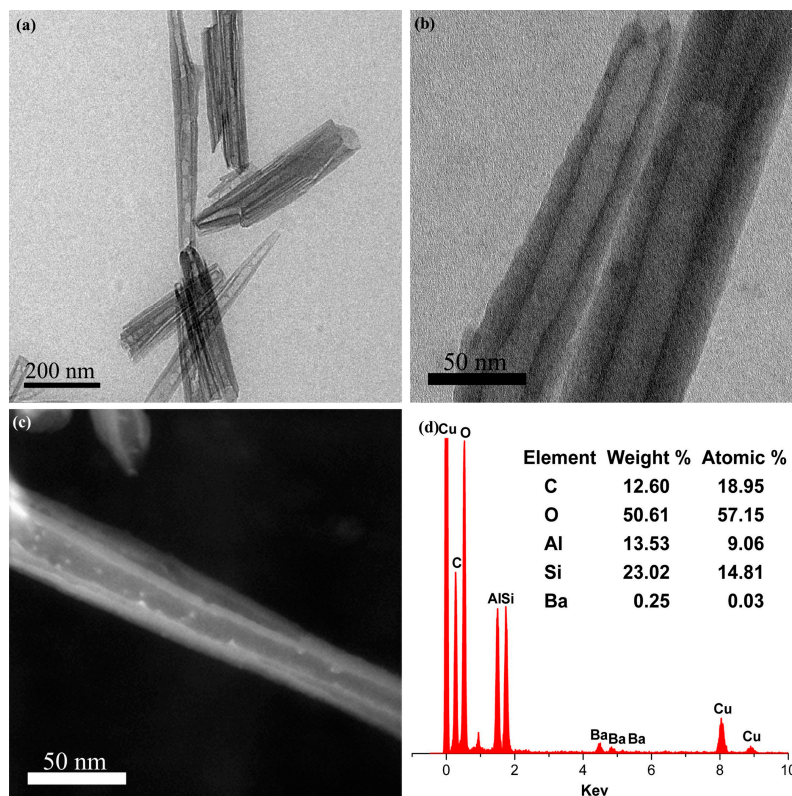
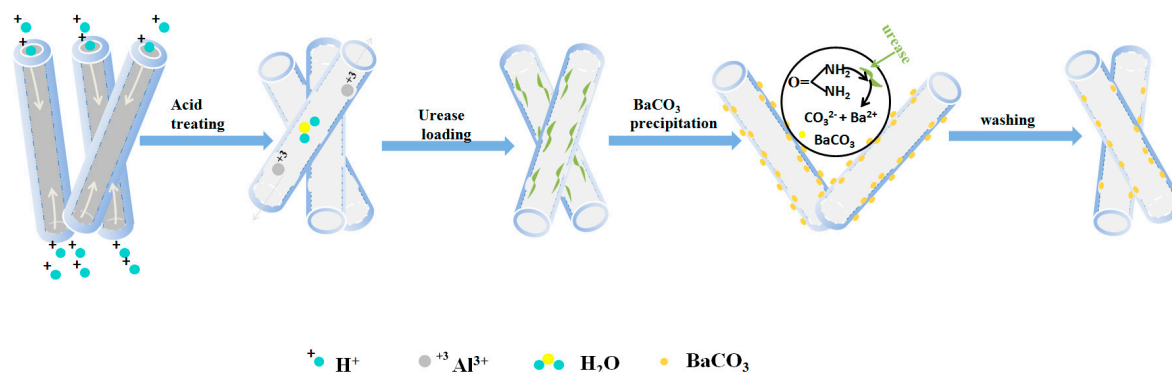


Figure 6. Morphologies of the samples. TEM images of (a) Hal, (b) A-Hal, (c) BaCO₃/A-Hal-T and (d) EDX spectrum of BaCO₃/A-Hal-T.

4. Assembly Mechanism Analysis

Based on the aforementioned results, a schematic illustration to describe the formation mechanism of the BaCO₃/A-Hal product is summarized in Scheme 1. During acid leaching, H⁺ gradually replaces the six-fold coordinated cations such as Al³⁺ and Fe³⁺ in the octahedral layer, which produces some defects through etching some Al³⁺ or [AlO₆] groups from the crystal lattice of the interior lumen, thus the Al content in each aluminosilicate layer is reduced, resulting in an increased interior tube diameter. The defects may also facilitate the selective adsorption of the Ba²⁺ metal cations [58]. The Hal is then dispersed in a urease solution, after the air in the Hal chamber is removed with a vacuum pump, the urease solvent is absorbed into the lumen. Since the isoelectric point of urease is pH ~6.0, the negative charged urease in distilled water can also be adsorbed and anchored into the lumen of Hal because of the positively charged interior surface [20]. After washing, excessive urease is eliminated from the outer surface due to the negatively charged status of this side. When the urea and Ba²⁺ solvent is absorbed into the lumen, the ureases will catalyze the decomposition of urea at a suitable temperature to produce ammonia and CO₃^{2−} ions and results in the alkaline environment in Hal lumen that promotes the formation of BaCO₃ nanoparticles within the lumen by inhibiting the hydrolysis of carbonate. Then the barium cations in the lumen will be coordinated by the carbonate radicals, finally yielding the BaCO₃ nanoparticles in situ inside the A-Hal lumen.



Scheme 1. Schematic illustration to the acid etching of Hal, and urease immobilization to catalyze the synthesis of barium carbonate in the lumen of A-Hal.

5. Conclusions

BaCO₃ nanoparticles were selectively synthesized in the lumen of nanotubes from natural halloysite for the first time. In the acid leaching process, the inner diameter of the halloysite tube was expanded, resulting in increased defect sites and zeta potential. Negatively charged urease and positively charged Hal lumens can form interactions, so urease was loaded into the lumens of Hal nanotubes. After barium cations and urea were absorbed from the surrounding solution, the ureases catalyzed the decomposition of urea to produce ammonia and CO₃^{2−} ions. BaCO₃ nanoparticles with sizes less than 8 nm were successfully loaded in situ in the A-Hal lumen, rather than loading the outer surface of the A-Hal. The channels of halloysite effectively confined the growth of BaCO₃ crystals and controlled geometrical morphology. The product had potential utilization in catalysis.

Author Contributions: J.O., D.M., Y.Z. conceived and designed the experiments; D.M. performed the experiments, analyzed the data and wrote the drafts of the paper; J.O., Y.Z., H.Y. and S.L.S. helped in the preparation of the paper and in checking, revising the drafts of the paper.

Funding: This work was supported by the National Natural Science Fund of China (51774331, 51374250), National dandong Science Fund for Distinguished Young Scholars (51225403), the Natural Science Fund of Hunan Province (2017JJ0351), the Innovation Driven Plan of Central South University (No. 2016CX015), the ShengHua Scholar Project of CSU (20160201), the Strategic Priority Research Program of Central South University (ZLXD2017005), the Fundamental Research Funds for the Central Universities of Central South University (2017zzts668, 2017zzts583 and 2017zzts436).

Conflicts of Interest: The authors declare no conflict of interest.

References

1. Zhang, Y.; Tang, A.; Yang, H.; Ouyang, J. Applications and interfaces of halloysite nanocomposites. *Appl. Clay Sci.* **2016**, *119*, 8–17. [[CrossRef](#)]
2. Yuan, P. Chapter 7—Thermal-Treatment-Induced Deformations and Modifications of Halloysite. *Dev. Clay Sci.* **2016**, *7*, 137–166.
3. Vinokurov, V.A.; Stavitskaya, A.V.; Chudakov, Y.A.; Ivanov, E.V.; Shrestha, L.K.; Ariga, K.; Darrat, Y.A.; Lvov, Y.M. Formation of metal clusters in halloysite clay nanotubes. *Sci. Technol. Adv. Mater.* **2017**, *18*, 147–151. [[CrossRef](#)] [[PubMed](#)]
4. Leporatti, S. Halloysite clay nanotubes as nano-bazookas for drug delivery. *Polym. Int.* **2017**, *66*, 1111–1118. [[CrossRef](#)]
5. García, F.J.; García Rodríguez, S.; Kalytta, A.; Reller, A. Study of Natural Halloysite from the Dragon Mine, Utah (USA). *Z. Anorg. Allg. Chem.* **2009**, *635*, 790–795. [[CrossRef](#)]
6. Massaro, M.; Cavallaro, G.; Colletti, C.G.; D’Azzo, G.; Guernelli, S.; Lazzara, G.; Pieraccini, S.; Riela, S. Halloysite nanotubes for efficient loading, stabilization and controlled release of insulin. *J. Colloid Interface Sci.* **2018**, *524*, 156–164. [[CrossRef](#)] [[PubMed](#)]

7. Ouyang, J.; Zhou, Z.; Zhang, Y.; Yang, H. High morphological stability and structural transition of halloysite (Hunan, China) in heat treatment. *Appl. Clay Sci.* **2014**, *101*, 16–22. [[CrossRef](#)]
8. Jin, J.; Zhang, Y.; Ouyang, J.; Yang, H. Halloysite nanotubes as hydrogen storage materials. *Phys. Chem. Miner.* **2013**, *41*, 323–331. [[CrossRef](#)]
9. Jin, J.; Fu, L.; Yang, H.; Ouyang, J. Carbon hybridized halloysite nanotubes for high-performance hydrogen storage capacities. *Sci. Rep.* **2015**, *5*, 12429. [[CrossRef](#)] [[PubMed](#)]
10. Wang, X.; Weiner, M.L. Hydrogen Storage Apparatus Comprised of Halloysite. U.S. Patent 7,425,232 B2, 16 September 2008.
11. Ouyang, J.; Zhao, Z.; Zhang, Y.; Yang, H. Textual properties and catalytic performances of halloysite hybrid CeO₂-ZrO₂ nanoparticles. *J. Colloid Interface Sci.* **2017**, *505*, 430–436. [[CrossRef](#)] [[PubMed](#)]
12. Zhang, Y.; He, X.; Ouyang, J.; Yang, H. Palladium nanoparticles deposited on silanized halloysite nanotubes: Synthesis, characterization and enhanced catalytic property. *Sci. Rep.* **2013**, *3*, 2948. [[CrossRef](#)] [[PubMed](#)]
13. Zeng, X.; Wang, Q.; Wang, H.; Yang, Y. Catalytically active silver nanoparticles loaded in the lumen of halloysite nanotubes via electrostatic interactions. *J. Mater. Sci.* **2017**, *52*, 8391–8400. [[CrossRef](#)]
14. Massaro, M.; Colletti, C.G.; Lazzara, G.; Milioto, S.; Noto, R.; Riela, S. Halloysite nanotubes as support for metal-based catalysts. *J. Mater. Chem. A* **2017**, *5*, 13276–13293. [[CrossRef](#)]
15. Wang, P.; Lv, A.; Hu, J.; Xu, J.A.; Lu, G. In Situ Synthesis of SAPO-34 Grown onto Fully Calcined Kaolin Microspheres and Its Catalytic Properties for the MTO Reaction. *Ind. Eng. Chem. Res.* **2011**, *50*, 9989–9997. [[CrossRef](#)]
16. Zhang, Y.; Yang, H. Zns/halloysite nanocomposites: Synthesis, characterization and enhanced photocatalytic activity. *Funct. Mater. Lett.* **2013**, *6*, 50013. [[CrossRef](#)]
17. Zhou, Z.; Ouyang, J.; Yang, H.; Tang, A. Three-way catalytic performances of Pd loaded halloysite-Ce_{0.5}Zr_{0.5}O₂ hybrid materials. *Appl. Clay Sci.* **2016**, *121–122*, 63–70. [[CrossRef](#)]
18. Ouyang, J.; Zhao, Z.; Yang, H.; Zhang, Y.; Tang, A. Large-scale synthesis of sub-micro sized halloysite-composed CZA with enhanced catalysis performances. *Appl. Clay Sci.* **2018**, *152*, 221–229. [[CrossRef](#)]
19. Ouyang, J.; Guo, B.; Fu, L.; Yang, H.; Hu, Y.; Tang, A.; Long, H.; Jin, Y.; Chen, J.; Jiang, J. Radical guided selective loading of silver nanoparticles at interior lumen and out surface of halloysite nanotubes. *Mater. Des.* **2016**, *110*, 169–178. [[CrossRef](#)]
20. Shchukin, D.G.; Sukhorukov, G.B.; Price, R.R.; Lvov, Y.M. Halloysite nanotubes as biomimetic nanoreactors. *Small* **2005**, *1*, 510–513. [[CrossRef](#)] [[PubMed](#)]
21. Zheng, P.; Du, Y.; Ma, X. Selective fabrication of iron oxide particles in halloysite lumen. *Mater. Chem. Phys.* **2015**, *151*, 14–17. [[CrossRef](#)]
22. Zahidah, K.A.; Kakooei, S.; Ismail, M.C.; Bothi Raja, P. Halloysite nanotubes as nanocontainer for smart coating application: A review. *Prog. Org. Coat.* **2017**, *111*, 175–185. [[CrossRef](#)]
23. Shu, Z.; Zhang, Y.; Yang, Q.; Yang, H. Halloysite Nanotubes Supported Ag and ZnO Nanoparticles with Synergistically Enhanced Antibacterial Activity. *Nanoscale Res. Lett.* **2017**, *12*, 135. [[CrossRef](#)] [[PubMed](#)]
24. Li, X.; Yang, Q.; Ouyang, J.; Yang, H.; Chang, S. Chitosan modified halloysite nanotubes as emerging porous microspheres for drug carrier. *Appl. Clay Sci.* **2016**, *126*, 306–312. [[CrossRef](#)]
25. Lun, H.; Ouyang, J.; Yang, H. Natural halloysite nanotubes modified as an aspirin carrier. *RSC Adv.* **2014**, *4*, 44197–44202. [[CrossRef](#)]
26. Shu, Z.; Zhang, Y.; Ouyang, J.; Yang, H. Characterization and synergetic antibacterial properties of ZnO and CeO₂ supported by halloysite. *Appl. Surf. Sci.* **2017**, *420*, 833–838. [[CrossRef](#)]
27. Makaremi, M.; Pasbakhsh, P.; Cavallaro, G.; Lazzara, G.; Aw, Y.K.; Lee, S.M.; Milioto, S. Effect of Morphology and Size of Halloysite Nanotubes on Functional Pectin Bionanocomposites for Food Packaging Applications. *ACS Appl. Mater. Interfaces* **2017**, *9*, 17476–17488. [[CrossRef](#)] [[PubMed](#)]
28. Hou, K.; Zeng, Y.; Zhou, C.; Chen, J.; Wen, X.; Xu, S.; Cheng, J.; Lin, Y.; Pi, P. Durable underwater superoleophobic PDDA/halloysite nanotubes decorated stainless steel mesh for efficient oil–water separation. *Appl. Surf. Sci.* **2017**, *416*, 344–352. [[CrossRef](#)]
29. Ganganboina, A.B.; Chowdhury, A.D.; Doong, R. New Avenue for Appendage of Graphene Quantum Dots on Halloysite Nanotubes as Anode Materials for High Performance Supercapacitors. *ACS Sustain. Chem. Eng.* **2017**, *5*, 4930–4940. [[CrossRef](#)]

30. Cavallaro, G.; Danilushkina, A.A.; Evtugyn, V.G.; Lazzara, G.; Milioto, S.; Parisi, F.; Rozhina, E.V.; Fakhrullin, R.F. Halloysite Nanotubes: Controlled Access and Release by Smart Gates. *Nanomaterials* **2017**, *7*, 199. [[CrossRef](#)] [[PubMed](#)]
31. Liu, S.; Zhang, Q.; Yang, H.; Mu, D.; Pan, A.; Liang, S. Fabrication of si nanoparticles@carbon fibers composites from natural nanoclay as an advanced lithium-ion battery flexible anode. *Minerals* **2018**, *8*, 180. [[CrossRef](#)]
32. Lu, Y.; Wang, L.; Preuß, K.; Qiao, M.; Titirici, M.-M.; Varcoe, J.; Cai, Q. Halloysite-derived nitrogen doped carbon electrocatalysts for anion exchange membrane fuel cells. *J. Power Sources* **2017**, *372*, 82–90. [[CrossRef](#)]
33. Niu, M.; Yang, H.; Zhang, X.; Wang, Y.; Tang, A. Amine-Impregnated Mesoporous Silica Nanotube as an Emerging Nanocomposite for CO₂ Capture. *ACS Appl. Mater. Interfaces* **2016**, *8*, 17312–17320. [[CrossRef](#)] [[PubMed](#)]
34. Lun, H.; Ouyang, J.; Yang, H. Enhancing dispersion of halloysite nanotubes via chemical modification. *Phys. Chem. Miner.* **2013**, *41*, 281–288. [[CrossRef](#)]
35. Zhang, H. Selective modification of inner surface of halloysite nanotubes: A review. *Nanotechnol. Rev.* **2017**, *6*. [[CrossRef](#)]
36. Chao, C.; Liu, J.; Wang, J.; Zhang, Y.; Zhang, B.; Zhang, Y.; Xiang, X.; Chen, R. Surface modification of halloysite nanotubes with dopamine for enzyme immobilization. *ACS Appl. Mater. Interfaces* **2013**, *5*, 10559–10564. [[CrossRef](#)] [[PubMed](#)]
37. Ropp, R.C. *Encyclopedia of the Alkaline Earth Compounds*; Elsevier: Amsterdam, The Netherlands, 2013; pp. 1179–1187.
38. Brightlin, B.C.; Balamurugan, S. Magnetic, Micro-structural, and Optical Properties of Hexaferrite, BaFe₁₂O₁₉ Materials Synthesized by Salt Flux-Assisted Method. *J. Superconduct. Nov. Magn.* **2016**, *30*, 215–225. [[CrossRef](#)]
39. Hong, T.; Chen, F.; Xia, C. Barium carbonate nanoparticle as high temperature oxygen reduction catalyst for solid oxide fuel cell. *Electrochem. Commun.* **2015**, *51*, 93–97. [[CrossRef](#)]
40. Hong, T.; Chen, F.; Xia, C. Barium carbonate nanoparticle to enhance oxygen reduction activity of strontium doped lanthanum ferrite for solid oxide fuel cell. *J. Power Sources* **2015**, *278*, 741–750. [[CrossRef](#)]
41. Cao, X.; Hong, T.; Yang, R.; Tian, J.-H.; Xia, C.; Dong, J.-C.; Li, J.-F. Insights into the Catalytic Activity of Barium Carbonate for Oxygen Reduction Reaction. *J. Phys. Chem. C* **2016**, *120*, 22895–22902. [[CrossRef](#)]
42. Cai, Z.; Zhang, Y.; Liu, T.; Huang, J. Mechanisms of Vanadium Recovery from Stone Coal by Novel BaCO₃/CaO Composite Additive Roasting and Acid Leaching Technology. *Minerals* **2016**, *6*, 26. [[CrossRef](#)]
43. Wang, Q.; Chen, J.; Han, K.; Wang, J.; Lu, C. Influence of BaCO₃ on chlorine fixation, combustion characteristics and KCl conversion during biomass combustion. *Fuel* **2017**, *208*, 82–90. [[CrossRef](#)]
44. Zhang, Q.; Chai, G.; Guo, Y.; Zhan, W.; Guo, Y.; Wang, L.; Wang, Y.; Lu, G. Gas-phase epoxidation of propylene by molecular oxygen over Ag-CuCl₂/BaCO₃ catalyst with low CuCl₂ doping: Catalytic performance, deactivation and regeneration. *J. Mol. Catal. A Chem.* **2016**, *424*, 65–76. [[CrossRef](#)]
45. Whittaker, M.L.; Smeets, P.J.M.; Asayesh-Ardakani, H.; Shahbazian-Yassar, R.; Joester, D. Multi-Step Crystallization of Barium Carbonate: Rapid Interconversion of Amorphous and Crystalline Precursors. *Angew. Chem. Int. Ed. Engl.* **2017**, *56*, 16028–16031. [[CrossRef](#)] [[PubMed](#)]
46. Massoni, N.; Le Gallet, S. Investigation of the sintering of barytocalcite with BaCO₃ as a secondary phase for immobilizing carbon-14. *J. Nucl. Mater.* **2016**, *476*, 13–19. [[CrossRef](#)]
47. Zhang, H.; Kong, W.; Tan, T.; Baeyens, J. High-efficiency concentrated solar power plants need appropriate materials for high-temperature heat capture, conveying and storage. *Energy* **2017**, *139*, 52–64. [[CrossRef](#)]
48. Disawal, S.; Qiu, J.; Elmore, B.B.; Lvov, Y.M. Two-step sequential reaction catalyzed by layer-by-layer assembled urease and arginase multilayers. *Colloids Surf. B Biointerfaces* **2003**, *32*, 145–156. [[CrossRef](#)]
49. Zhang, Q.; Yan, Z.; Ouyang, J.; Zhang, Y.; Yang, H.; Chen, D. Chemically modified kaolinite nanolayers for the removal of organic pollutants. *Appl. Clay Sci.* **2018**, *157*, 283–290. [[CrossRef](#)]
50. Fu, L.; Yang, H.; Tang, A.; Hu, Y. Engineering a tubular mesoporous silica nanocontainer with well-preserved clay shell from natural halloysite. *Nano Res.* **2017**, *10*, 2782–2799. [[CrossRef](#)]
51. Faiza, B.G.L. Surface and Interface Chemistry of Clay Minerals. In *Handbook of Clay Science*; Elsevier: Amsterdam, The Netherlands, 2013; pp. 147–150.
52. Li, Y.; Zhang, Y.; Zhang, Y.; Sun, J.; Wang, Z. Thermal behavior analysis of halloysite–dimethylsulfoxide intercalation complex. *J. Therm. Anal. Calorim.* **2017**, *129*, 985–990. [[CrossRef](#)]

53. Zhai, R.; Zhang, B.; Liu, L.; Xie, Y.; Zhang, H.; Liu, J. Immobilization of enzyme biocatalyst on natural halloysite nanotubes. *Catal. Commun.* **2010**, *12*, 259–263. [[CrossRef](#)]
54. Ouyang, J.; Mu, D.; Zhang, Y.; Yang, H. Mineralogy and Physico-Chemical Data of Two Newly Discovered Halloysite in China and Their Contrasts with Some Typical Minerals. *Minerals* **2018**, *8*, 108. [[CrossRef](#)]
55. Vial, S.; Forano, C.; Shan, D.; Mousty, C.; Barhoumi, H.; Martelet, C.; Jaffrezic, N. Nanohybrid-layered double hydroxides/urease materials: Synthesis and application to urea biosensors. *Mater. Sci. Eng. C* **2006**, *26*, 387–393. [[CrossRef](#)]
56. Yuan, P.; Tan, D.; Aannabi-Bergaya, F.; Yan, W.; Fan, M.; Liu, D.; He, H. Changes in structure, morphology, porosity, and surface activity of mesoporous halloysite nanotubes under heating. *Clays Clay Miner.* **2012**, *60*, 561–573. [[CrossRef](#)]
57. György, E.; Sima, F.; Mihailescu, I.N.; Smausz, T.B.; Hopp, D.; Predoi, L.E.; Sima, S.M. Biomolecular urease thin films grown by laser techniques for blood diagnostic applications. *Mater. Sci. Eng. C* **2010**, *30*, 537–541.
58. Abdullayev, E.; Joshi, A.; Wei, W.; Zhao, Y.; Lvov, Y. Enlargement of halloysite clay nanotube lumen by selective etching of aluminum oxide. *ACS Nano* **2012**, *6*, 7216–7226. [[CrossRef](#)] [[PubMed](#)]



© 2018 by the authors. Licensee MDPI, Basel, Switzerland. This article is an open access article distributed under the terms and conditions of the Creative Commons Attribution (CC BY) license (<http://creativecommons.org/licenses/by/4.0/>).